Materials Today Energy 18 (2020) 100529

Contents lists available at ScienceDirect

Materials Today Energy

journal homepage: www.journals.elsevier.com/materials-today-energy/

Introducing Na_2SO_4 in aqueous $ZnSO_4$ electrolyte realizes superior electrochemical performance in zinc-ion hybrid capacitor

K.A. Owusu [a], X. Pan [a], R. Yu [a], L. Qu [b], Z. Liu [a], Z. Wang [a], M. Tahir [a], W.A. Haider [a], L. Zhou [a, *], L. Mai [a, c, **]

[a] State Key Laboratory of Advanced Technology for Materials Synthesis and Processing, Wuhan University of Technology, Wuhan, 430070, China
[b] Department of Mechanical Engineering, The University of Melbourne, Parkville, VIC, 3010, Australia
[c] Foshan Xianhu Laboratory of the Advanced Energy Science and Technology Guangdong Laboratory, Xianhu Hydrogen Valley, Foshan, 528200, China

ARTICLE INFO

Article history:
Received 29 June 2020
Received in revised form
2 September 2020
Accepted 3 September 2020
Available online 24 September 2020

Keywords:
Zn-ion hybrid capacitor
Charge storage mechanism
Aqueous electrolyte
Activated carbon cloth
Proton adsorption/desorption

ABSTRACT

Zinc-ion hybrid capacitors (ZIHCs) are gaining much attention for their high energy density; however, the charge storage in traditional $ZnSO_4$ electrolyte is limited by its low ionic conductivity, resulting in low specific capacity, rate capability, and gravimetric energy/power density at high rates. Herein, we report a ZIHC with high charge storage, enhanced rate capability, and superior energy/power density by introducing Na_2SO_4 in the traditional $ZnSO_4$ electrolyte. The addition of Na_2SO_4 contributes immensely to the enhancement of capacitive charge storage in the activated carbon cloth positive electrode at high rates and shields the zinc anode from dendrite formation, resulting in excellent electrochemical performance. Specifically, the ZIHC with $ZnSO_4/Na_2SO_4$ electrolyte presents high electrical and ionic conductivity, high specific capacity (152 mAh g^{-1}), improved rate capability, and gravimetric energy density (20 Wh kg^{-1} at 1692 W kg^{-1}). In contrast, the ZIHC with traditional $ZnSO_4$ electrolyte delivers a much lower energy density at high rate (4.5 Wh kg^{-1} at 50 mA cm^{-2}). In-situ Raman, nuclear magnetic resonance, and ex-situ X-ray diffraction demonstrate the inclusion of proton adsorption/desorption in the charge storage process. The proton storage process plays a vital role in the formation/dissolution of $Zn(OH)_2$ analogs, extension of the voltage window to 1.9 V without compromising the Coulombic efficiency and overall charge storage. This article highlights the importance of electrolyte modification for enhancing the electrochemical performances of ZIHCs.

1. Introduction

Energy storage has gained immense research attention over the past two decades owing to the need to decarbonize our energy system and meet the goals of the Paris Agreement [1–3]. Solar and wind energy are regarded as potential replacements for fossil fuels, but their seasonal characteristic requires the development of high-performance energy storage devices. Among the different energy storage devices, supercapacitor, a device characterized by high power density (1–10 kW kg^{-1}), fast charge/discharge rates, and stable cycling performances (>100,000 cycles), holds great potential [2,4–7]. Different types of supercapacitors, including electric double-layer capacitors, pseudocapacitors, and asymmetric supercapacitors, have been extensively studied with the aims of improving the energy density [8–13]. However, the attained energy density of supercapacitors is still one to two orders of magnitude lower than lithium-ion batteries (LIBs) [14]. In the past few years, metal-ion hybrid capacitors, notably lithium-ion hybrid capacitors, have been studied extensively to achieve the best trade-off between supercapacitors and LIBs [15–18]. However, several key challenges such as the limited energy storage of univalent ion-based systems and the rising costs of lithium resources have curtailed present interest. Notwithstanding, the development of other metal-ion hybrid capacitors with better chemistries are still needed [14,19].

Presently, multivalent zinc ion storage in batteries and supercapacitors is a rapid-developing research area owing to its many

* Corresponding author.
** Corresponding author. State Key Laboratory of Advanced Technology for Materials Synthesis and Processing, Wuhan University of Technology, Wuhan, 430070, China.
E-mail addresses: liangzhou@whut.edu.cn (L. Zhou), mlq518@whut.edu.cn (L. Mai).

https://doi.org/10.1016/j.mtener.2020.100529
2468-6069/

desirable advantages such as the large theoretical capacity of Zn (823 mAh g^{-1}), low redox potential, cost-effectiveness, excellent stability, safety, and suitability for practical applications [20–26]. Zinc-ion hybrid capacitors (ZIHCs) mostly use a high surface area carbon as the positive electrode and metallic zinc as the negative electrode in $ZnSO_4$ electrolyte [19,22,27,28]. Despite the advances, the mass loading of activated carbon-based positive electrode in most reported ZIHCs is extremely low ($\leq$2 mg cm^{-2}), which is not ideal for practical applications [22,29]. Furthermore, the selection of $ZnSO_4$ electrolyte for ZIHCs is limited by several peculiar challenges, namely low Coulombic efficiency, poor rate capability due to side reactions and formation of Zn dendrites, limited voltage windows, etc. [22,30–32]. $Zn(CF_3SO_3)_2$-based electrolytes have been successfully used in ZIHCs to achieve high Coulombic efficiency and inhibit side reactions; however, it is 20 times more expensive than the $ZnSO_4$ electrolytes [27,33]. A more effective strategy would be the modification of $ZnSO_4$ electrolytes to achieve improved performance. By adding Na_2SO_4 to $ZnSO_4$ electrolyte, Chen and co-workers successfully enhanced the cycling performance of Zn//sodium vanadate batteries [34]. Long and co-workers revealed that the Na^+ enabled pseudocapacitance would lead to increased charge storage and rate capability in MnO_x electrodes in mixed $Na_2SO_4/ZnSO_4$ electrolytes [35,36]. However, the charge storage process in carbon materials is totally different from that of MnO_x, and the effect of a mixed electrolyte on the electrochemical performance is yet to be studied. In addition, carbon exhibits excellent rate capability and wide potential windows in Na_2SO_4 and LiCl electrolytes [37]. Hence, a mixed electrolyte is expected to boost the electrochemical performance of ZIHCs. Finally, the charge storage mechanism occurring in ZIHCs is still inconclusive, requiring further research attention.

Herein, we report an activated carbon cloth–based ZIHC (ACC//Zn ZIHC) using aqueous $ZnSO_4/Na_2SO_4$ electrolyte with boosted electrochemical performance. The ACC cathode (13 mg cm^{-2}) is characterized by edge-rich, high oxygen functionalization, high surface area, which endow the material exceptional charge storage. Firstly, we prove that the addition of 1 M Na_2SO_4 into traditional 1 M $ZnSO_4$ electrolyte inhibits the growth of $Zn_4SO_4(OH)_6{\cdot}0.5H_2O$ for Zn anode protection and enhances the capacitive charge storage at high rates in the ACC positive electrode (Fig. 1). This results in lowered resistances, a substantial reduction in voltage drop, enhanced charge storage at high current densities, and greater gravimetric energy/power density. Based on this, the fabricated ACC//Zn ZIHC with the $ZnSO_4/Na_2SO_4$ electrolyte can operate in a 1.9 V wide voltage window and achieves energy densities of 100 and 20 Wh kg^{-1} at 50.42 and 1692 W kg^{-1}, respectively. In contrast, the energy/power density of the ZIHC with $ZnSO_4$ electrolyte alone is much lower at high rates (4.6 Wh kg^{-1} at 881 W kg^{-1}). Through X-ray diffraction (XRD), X-ray photoelectron spectroscopy (XPS), nuclear magnetic resonance (NMR), and Raman spectroscopy, we revealed the H^+ electro-adsorption/desorption contribution to the total double-layer capacitance in the ZIHCs, which has been overlooked in previous studies. The incorporation of H^+ to the total charge storage plays a pivotal role in extending the cell voltage (from 0.2–1.8 V to 0–1.9 V) without compromising the Coulombic efficiency. To demonstrate the universality of this electrolyte modification strategy, ZIHCs with 1 M LiCl/1 M $ZnSO_4$ electrolyte are also assembled, and they also demonstrate high energy/power density as well as improved rate capability.

2. Experimental section

2.1. Synthesis of activated carbon cloth

The ACC was synthesized by a recently reported method with slight modifications [38]. In brief, carbon clothes (CCs) were first soaked in a mixed solution of 20 mL H_2SO_4 and 10 mL HNO_3 in a capped container for 12 h at room temperature. Afterward, the acid-treated CCs were washed with deionized water for several times. Next, the CCs were annealed in air at 400 °C for 6 h with a heating rate of 2 °C/min. The mass density of the ACC is determined to be 13 mg cm^{-2}.

2.2. Material characterization

Scanning electron microscopy (SEM) images were recorded using a JEOL-7100F microscope. Transmission electron microscopy (TEM) images were obtained with a JEM-2100F microscope. In-situ Raman spectra were collected using a Renishaw INVIA micro-Raman spectroscopy system. The Brunauer–Emmett–Teller (BET) surface area was measured using a Tristar II 3020 instrument at 77 K. XPS analysis was conducted using a VG Multi Lab 2000 instrument. Solid-state ^1H NMR measurements were conducted with a Bruker Advance III HD 600. XRD patterns were obtained with a Bruker D8 Discover X-ray diffractometer with a Cu Kα X-ray (λ = 1.5418 Å) at room temperature.

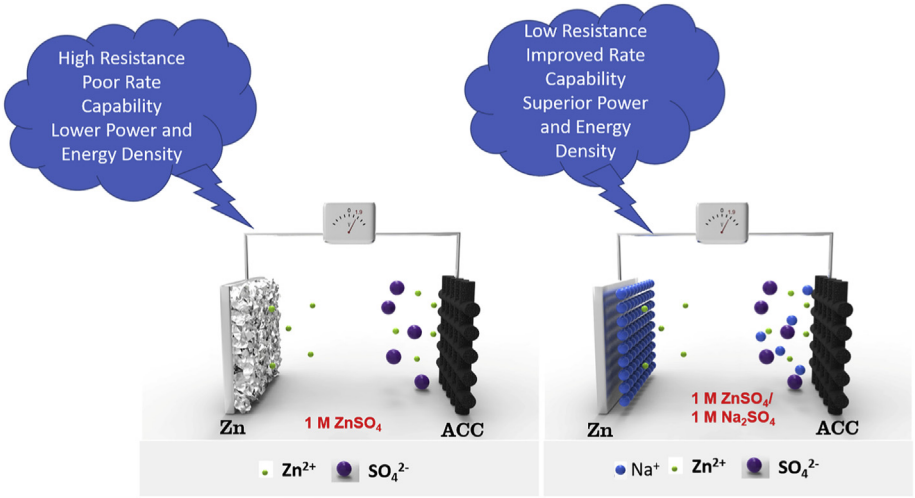

Fig. 1. Schematic representation of the ZIHC with Zn foil anode and ACC positive cathode with $ZnSO_4$ electrolyte (left) and mixed $ZnSO_4/Na_2SO_4$ electrolyte (right).

2.3. Electrochemical characterization

The electrochemical measurements were tested with a CHI 760E electrochemical workstation. ZIHCs were fabricated with ACC cathode, zinc foil anode, NKK separator, and 1 M $ZnSO_4$, 1 M $ZnSO_4$/1 M Na_2SO_4 or 1 M $ZnSO_4$/1 M LiCl aqueous solution as the electrolyte. For control, symmetric supercapacitors using ACC in 1 M Na_2SO_4, 1 M Na_2SO_4/1 M $ZnSO_4$, and 1 M $ZnSO_4$ electrolytes were also fabricated. Electrochemical impedance spectroscopy (EIS) was performed under a sinusoidal signal at open circuit potential over a frequency range from 0.01 to 10^5 Hz with a magnitude of 10 mV.

2.4. Calculations

Calculation of the specific capacity of ZIHCs: The specific capacity of ZIHCs at various current densities were calculated from the galvanostatic charge/discharge (GCD) curves using the equation shown below.

$$C_g = \frac{I\Delta t}{3.6m} \tag{1}$$

where $C\ (mA\ h\ g^{-1})$ is the specific capacity, $I\ (A)$ is the discharge current, $\Delta t\ (s)$ is the discharge time, and m is the mass of the electrode.

Calculation of energy and power density of the supercapacitors: The energy and power densities of the ZIHCs were calculated using the equations below:

$$E = \frac{1}{M}\int_0^{t_d} IVdt \tag{2}$$

$$P = \frac{3600E}{\Delta t} \tag{3}$$

where $E\ (Wh\ kg^{-1})$ is the energy density, $P\ (W\ kg^{-1})$ is the power density, $M\ (g)$ is the mass of the cathode material, I is the current density (A), V is the operating voltage window of the supercapacitor, and $\Delta t\ (s)$ is the discharge time.

The maximum power densities of the ZIHCs were calculated using the equations shown below:

$$IR_{drop} = a + bI \tag{4}$$

$$P_{max} = \frac{V_{applied}^2}{4R_s} = \frac{(V_{applied} - a)^2}{2b} \tag{5}$$

where a is the voltage difference between the applied voltage ($V_{applied}$) and the real voltage of the device or electrode and b represents twice the value of the equivalent series resistance (ESR).

3. Results and discussion

The ACC cathode was prepared by a recently reported activation method [38]. As demonstrated in our previous report, calcination of CCs in air is a facile and effective strategy to activate the CC, endowing the material rich O-containing functional groups, large surface area, and rich microporosity. The surface morphology of ACC was studied using SEM. As shown in Fig. 2a, the ACC possesses a very rough surface with abundant protrusions. High-magnification SEM image reveals that the surface of ACC is highly porous with loosely exfoliated graphene-like nanosheets (Fig. 2b) [39]. In contrast, the pristine CC possesses a smooth surface (Fig. S1). Next, TEM was used to obtain detailed information on the microstructure of ACC [40,41]. The TEM image (Fig. 2c) shows that the ACC possesses a loose carbon nanosheet shell over a relatively compact carbon core. From the HRTEM image (Fig. 2d), it is evident that the carbon nanosheets are mostly scrolled with lattice spacings of 0.34 nm which matches very well with the (002) d-spacing of graphitic carbon. The high-angle annular dark field-scanning transmission electron microscopy (HAADF-STEM) image in Fig. 2e confirms that the ACC has a core shell structure with a highly porous surface (Fig. 2e). Besides, the HAADF-STEM images and corresponding elemental mapping (Fig. 2f and g) clearly confirms the edge-rich, oxygen functionalization of the ACC.

N_2 sorption analysis was conducted to determine the surface area and porosity of ACC. The ACC displays a typical type-I isotherm with an H4 hysteresis loop (Fig. 2h) [42–44]. The ACC possesses a high BET surface area of 745 $m^2\ g^{-1}$. The type-I isotherm is characterized for microporous materials, which can be confirmed by the pore size distribution (PSD). In contrast, the pristine CC presents a small surface area of 0.8 $m^2\ g^{-1}$ (Fig. S2) suggesting its nonporous feature.

Next, the elemental composition of the ACC was determined using XPS. The survey spectrum reveals the presence of carbon, oxygen, and a trace amount of nitrogen (Fig. S3a). The C 1s peak can be deconvoluted into four peaks, namely, C–C, C–OH/C–N, C=O, and COOH with binding energies of 284.79, 285.85, 287.10, and 290.24 eV, respectively (Fig. S3b) [38,40,41]. The deconvolution of the O1s core-level spectrum results in four peaks: carbonyl oxygen of quinones (531.06 eV), carbonyl oxygen atoms in esters, anhydrides, and oxygen atoms in hydroxyl groups (532.10 eV), non-carbonyl oxygen atoms in esters and anhydrides (533.38 eV), and finally, oxygen atoms in carboxyl groups (534.05 eV), as depicted in Fig. S3c [38,40,41]. Lastly, the deconvolution of N 1s core-level spectrum reveals four peaks; namely, oxidized N (N-X), quaternary N (N-Q), pyrrolic N (N-5), and pyridinic N (N-6) peaks with binding energies of 403.4, 401.0, 399.6, and 398.6 eV, respectively (Fig. S3d) [45,46]. The surface N content in the activated CC is calculated to be 2.08 at.%.

To explore the electrochemical performance, ZIHCs were assembled using ACC positive electrode and zinc foil anode. The zinc foil stores charges Faradaically through a stripping-destripping process while the ACC positive electrode predominantly uses the adsorption of electrolyte ions to store charges [22,25,27]. Firstly, cyclic voltammetry (CV), rate capability, and EIS studies were adopted to reveal 1 M $ZnSO_4$/1 M Na_2SO_4 as the optimum electrolyte for ZIHCs (Fig. S4). The ionic conductivities of the various electrolyte combinations were further tested, confirming 1 M $ZnSO_4$/1 M Na_2SO_4 electrolyte as the most conductive electrolyte (Table S1). CV curves at various scan rates reveal that the Zn//ACC ZIHCs with both 1 M $ZnSO_4$ and 1 M $ZnSO_4$/1 M Na_2SO_4 electrolyte can achieve an ultrahigh voltage window of 1.9 V (Fig. S5). Comparatively, the ZIHC with $ZnSO_4$/Na_2SO_4 achieves higher current response with larger CV areas at various scan rates than the ZIHC with traditional $ZnSO_4$ electrolyte (Fig. 3a). Also, the ZIHC exhibits more obvious redox peaks in the $ZnSO_4$/Na_2SO_4 electrolyte than in traditional $ZnSO_4$ electrolyte. GCD analysis can provide more insights into the charge storage capability of the ZIHCs. Typical GCD curves at a high current density of 65 mA cm^{-2} reveals that the charge storage process is heavily suppressed in the $ZnSO_4$ electrolyte (Fig. 3b), indicating the high resistance in this electrolyte. To be specific, the internal resistance (IR) drops of the ZIHCs with $ZnSO_4$ and $ZnSO_4$/Na_2SO_4 electrolytes are 1.7 and 1.0 V, respectively. The trend of high resistance in $ZnSO_4$ electrolyte is observed at all current densities and this clearly reveals the substantial improvement of conductivity of the $ZnSO_4$ electrolyte by the introduction of Na_2SO_4 (Fig. S6). A lower IR drop in the modified

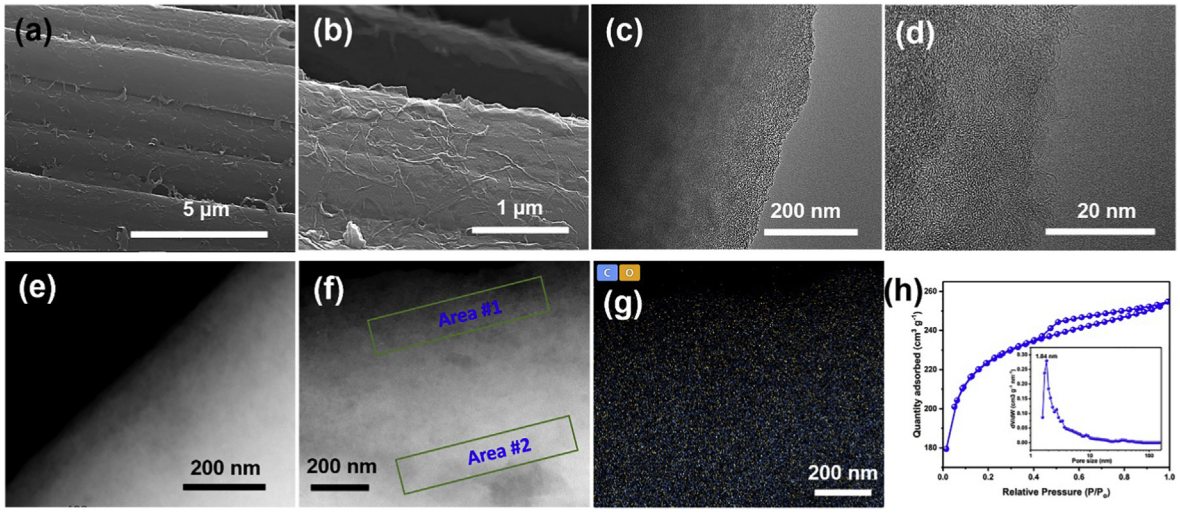

Fig. 2. (a) SEM image of ACC at low magnification; (b) SEM image of the ACC at high magnification; (c) TEM image of the ACC; (d) high-resolution TEM image of the ACC; (e–g) HAADF-STEM images with corresponding elemental mappings; (h) N_2 adsorption-desorption isotherm of the ACC (inset: PSD of the ACC).

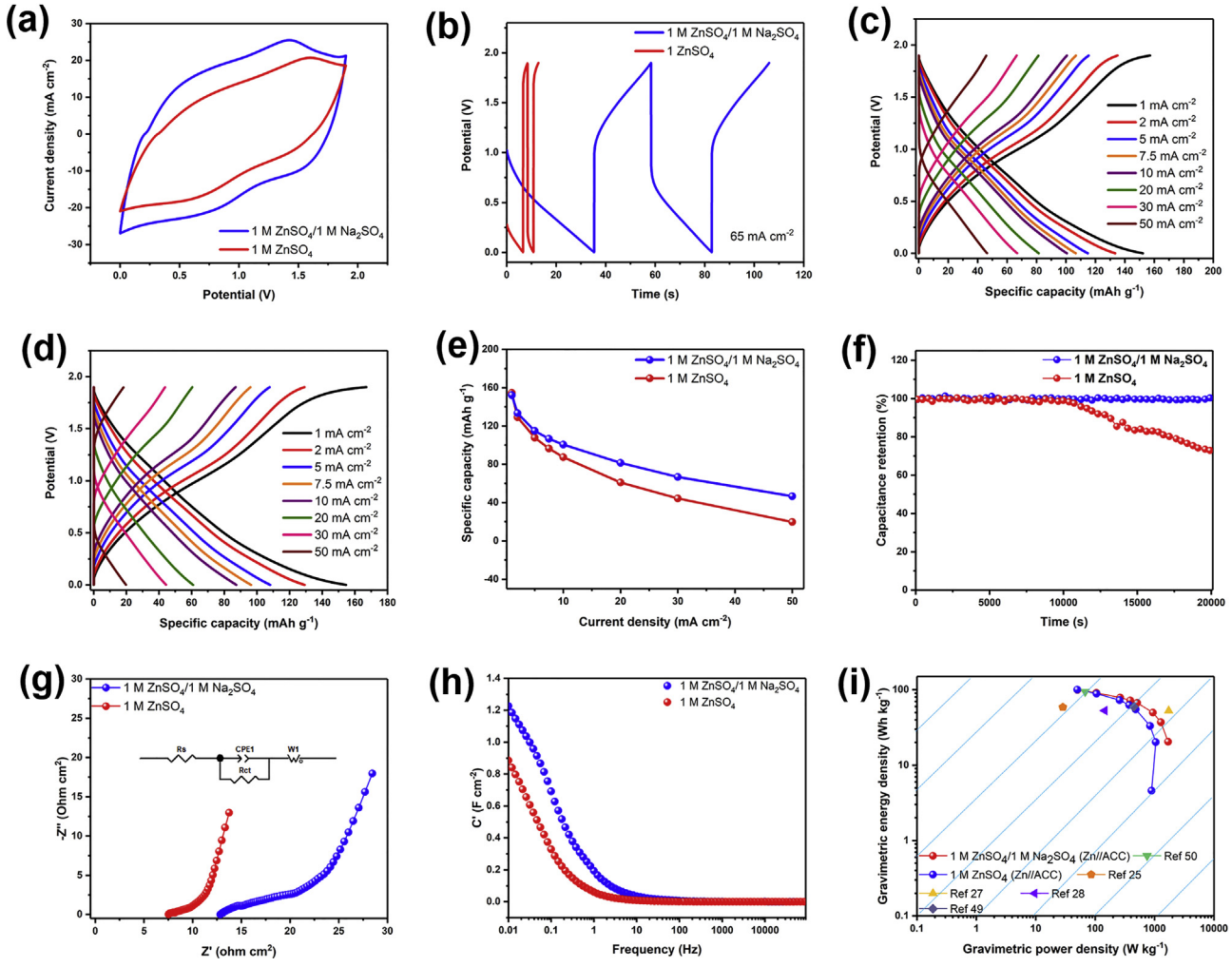

Fig. 3. (a) CV curves of the ZIHCs with 1 M $ZnSO_4$ and 1 M $ZnSO_4$/1 M Na_2SO_4 electrolytes. (b) GCD curves of the ZIHCs with 1 M $ZnSO_4$ and 1 M $ZnSO_4$/1 M Na_2SO_4 electrolytes. (c) GCD profiles of the ZIHC with $ZnSO_4$/Na_2SO_4 electrolyte at various current densities. (d) GCD profiles of the ZIHC with $ZnSO_4$ electrolyte at various current densities. (e) Rate performances of the ZIHCs with $ZnSO_4$ and $ZnSO_4$/Na_2SO_4 electrolytes. (f) Cycling performances of the ZIHCs with $ZnSO_4$/Na_2SO_4 and $ZnSO_4$ electrolytes. (g) Comparison of the Nyquist curves of the ZIHC in 1 M $ZnSO_4$ and 1 M $ZnSO_4$/1 M Na_2SO_4 electrolyte. (h) Real capacitance versus frequency in the two electrolytes. (i) Ragone plot of the Zn//ACC device in 1 M $ZnSO_4$/1 M Na_2SO_4 and 1 M Na_2SO_4. Other reported ZIHCs are added to the Ragone plot for comparison.

electrolyte is expected to impact positively on the rate capability, energy density, and power density of the Zn//ACC device. The rate capability of the ZIHCs with $ZnSO_4$ and $ZnSO_4/Na_2SO_4$ electrolytes are shown in Fig. 3c and d, respectively. As shown in Fig. 3e, the attained capacities in $ZnSO_4/Na_2SO_4$ electrolyte are 153, 133, 115, 107, 101, 82, 67, and 47 mAh g^{-1} at 1, 2, 5, 7.5, 10, 20, 30, and 50 mA cm^{-2}, respectively. In contrast, the ZIHC with traditional $ZnSO_4$ electrolyte exhibits lower rate capability with capacities of 154–19 mAh g^{-1} in the 1–50 mA cm^{-2} range. A major limitation of $ZnSO_4$ electrolytes compared with other zinc-containing electrolytes such as $Zn(CF_3SO_3)_2$ and $ZnCl_2$ is their inferior Coulombic efficiency [47]. However, the addition of Na_2SO_4 to $ZnSO_4$ electrolytes improves the Coulombic efficiency to 97–100% at different current densities (Fig. 3c). The long-term cycling performance is also tested and the ZIHC with the $ZnSO_4/Na_2SO_4$ electrolyte achieves stable cycling over 20,000 cycles (Fig. 3f). In contrast, the ZIHC with $ZnSO_4$ electrolyte shows obvious capacitance degradation.

To reveal the reasons for the improvement in rate capability and charge storage at high rates, EIS of the ZIHCs is provided. Fig. 4g shows a comparison of the Nyquist plots of the ZIHCs with $ZnSO_4$ and $ZnSO_4/Na_2SO_4$ electrolytes. The series resistance (R_s) is the summation of the inherent material resistance, ionic resistance, and the contact resistance at the electrode/electrolyte interface and can be obtained at the intercept of the real part of the EIS plot at high frequencies [48]. On the other hand, the charge transfer resistance (R_{ct}) is related to the resistance at the electrode–electrolyte interface during electron transfer and is obtained from the semi-circle of the Nyquist plot at high frequencies. It is obvious from Fig. 3g that the $ZnSO_4/Na_2SO_4$ electrolyte presents lower R_s and R_{ct}. A fitting of the EIS plot obtained in $ZnSO_4/Na_2SO_4$ electrolyte using the equivalent circuit (inset) reveals R_s and R_{ct} values of 7.2 and 4.2 Ω, compared with 12.3 and 6.2 Ω in the $ZnSO_4$ electrolyte. Moreover, a steeper slope is obtained in the low frequency region in $ZnSO_4/Na_2SO_4$ electrolyte, revealing that the addition of Na_2SO_4 results in faster diffusion kinetics. The frequency-dependent response of capacitance in $ZnSO_4$ and $ZnSO_4/Na_2SO_4$ electrolytes can be obtained from the Bode plot representations of the EIS spectra (Fig. 3h) [36]. The capacitance of ZIHC with $ZnSO_4/Na_2SO_4$ increases rapidly at 5 Hz and achieves a maximum value of 1.2 F cm^{-2}. As expected, a lower capacitance is achieved at low frequencies in the $ZnSO_4$ electrolyte.

The gravimetric energy and corresponding power density are calculated for the ZIHCs with different electrolytes. As shown in Fig. 3i, the gravimetric energy density of the ZIHC with $ZnSO_4/Na_2SO_4$ electrolyte reaches 100 Wh kg^{-1} at a power density of 43.89 W kg^{-1}. At high rates, the ZIHC retains a high energy density of 20.4 Wh kg^{-1} and a power density of 1692 W kg^{-1}, vastly exceeding the energy density and power density in $ZnSO_4$. Overall, the energy/power densities of the device surpass those of other ZIHCs (Table S2) [22,25,27,28,49,50]. The maximum gravimetric power density of a supercapacitor is mainly affected by the R_s and can be calculated based on the linear fit of the IR drop (Fig. S6). A maximum gravimetric power density of 112 kW kg^{-1} is determined for the ZIHC with $ZnSO_4/Na_2SO_4$ electrolyte.

The electrochemical performance of ZIHCs with $ZnSO_4$ electrolytes are mostly limited to a potential window of 0.2–1.8 V owing to water splitting (generation of oxygen and hydrogen). However, the Zn//ACC device is stable in an extended potential window of 0–1.9 V and displays excellent Coulombic efficiency, which eliminates the potential contribution of water splitting to charge storage. The CV curves of the ZIHCs exhibit obvious reversible humps at 0.75 and 1.35 V, signifying the possible inclusion of pseudocapacitance in the charge storage process. Previous studies have made attempts to explain the charge storage mechanism in ZIHCs; however, the underlying charge storage process is still unclear. Here, different diagnostic techniques have been used to study the charge storage process of ZIHCs (Fig. 4). Firstly, the ZIHCs are cycled for 200 times at 2 mV s^{-1}, and Fig. 4a shows the representative CV curves of the ZIHCs. A close observation of the CV curves divulges the gradual

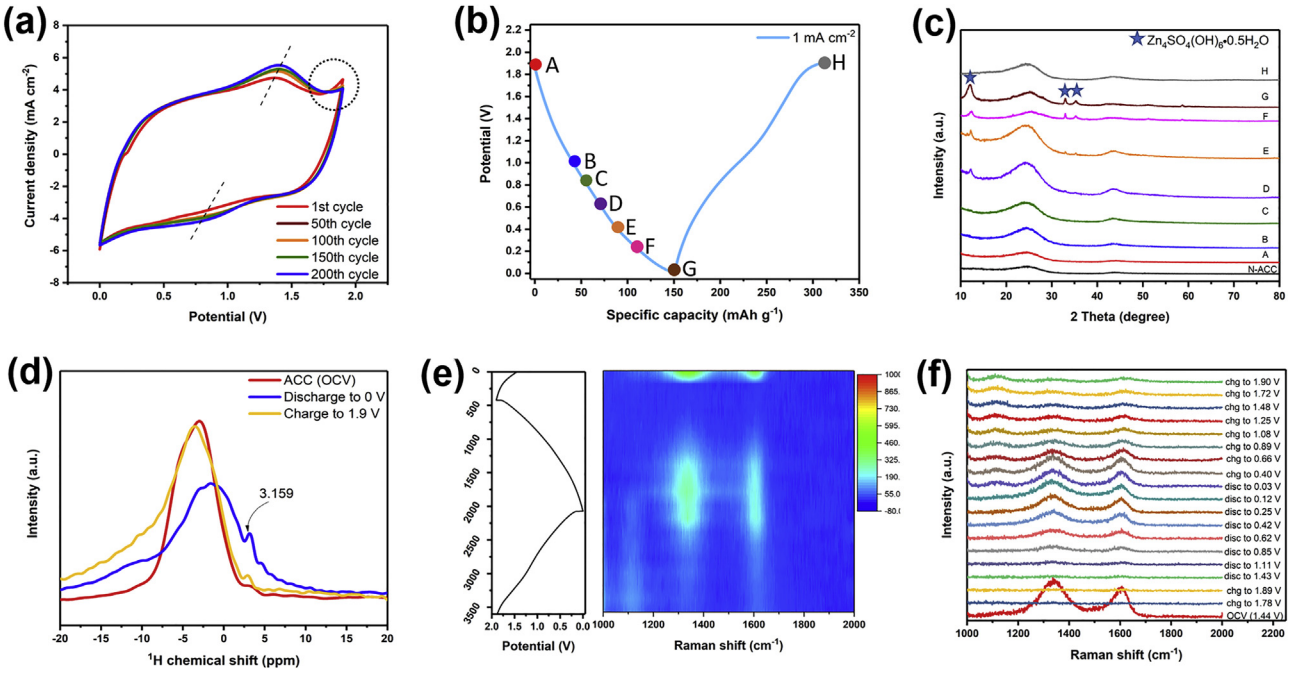

Fig. 4. CV curves of the ACC//Zn ZIHC with $ZnSO_4/Na_2SO_4$ at 1st, 50th, 100th, 150th, and 200th cycles (scan rate: 2 mV s^{-1}). (b) A GCD profile of the ACC//Zn ZIHC with $ZnSO_4/Na_2SO_4$ electrolyte at a current density of 1 mA cm^{-2}. (c) XRD patterns of the ACC cathode at different charge discharge states. (d) Solid-state ^1H NMR. (e) In-situ Raman spectra of the ACC cathode in $ZnSO_4/Na_2SO_4$ electrolyte. (f) Raman profiles at the different charge and discharge states.

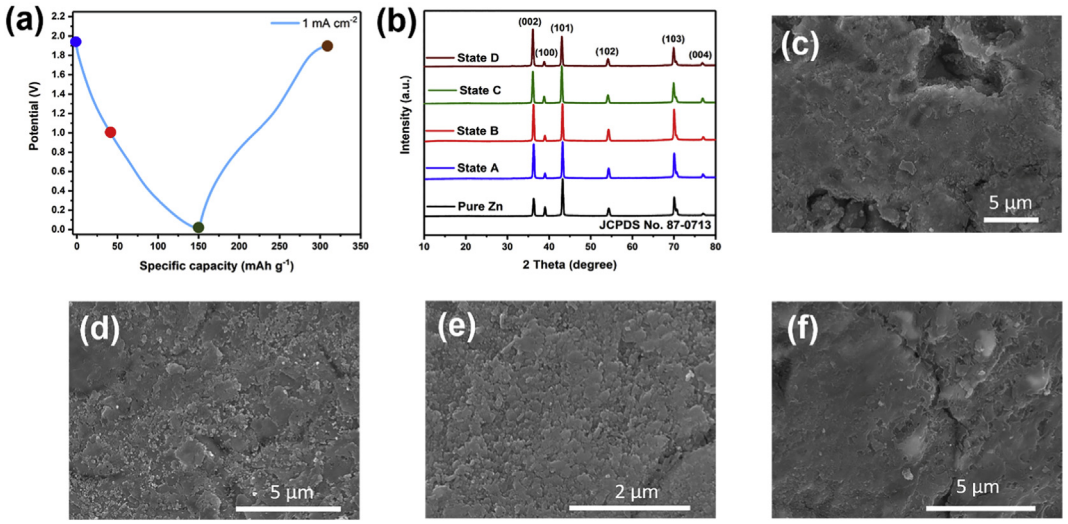

Fig. 5. (a) GCD profile of the ACC//Zn ZIHC with $ZnSO_4/Na_2SO_4$ electrolyte at a current density of 1 mA cm^{-2}. (b) XRD patterns of the Zn-foil anode at different charge/discharge states. (c) SEM image of the zinc foil after charged to 1.9 V (State A). (d) SEM image of the zinc foil after discharged to 1.0 V (State B). (e) SEM image of the zinc foil after discharged to 0 V (State C). (f) SEM image of the zinc foil after fully charged to 1.9 V (State D).

increase in CV area accompanied by suppressed water splitting approaching 1.9 V (indicated by a dashed black circle) with increasing cycles. To understand the underlying charge storage process, *ex-situ* XRD is performed at various charge-discharge points (A–H) as depicted in Fig. 4b. The ACC presents a typical amorphous-like XRD pattern which is still maintained during the first charge from open circuit voltage (1.44 V) to the maximum potential of 1.9 V (point A). The amorphous XRD pattern is still retained during the subsequent discharge process from 1.9 V until a potential of 0.6 V (state D), where a weak peak appears at 12.2°. The intensity of the 12.2° peak becomes stronger and other related peaks of $Zn_4SO_4(OH)_6{\cdot}0.5H_2O$ at 32.98° and 35.26° appear below 0.4 V until the final discharge potential of 0 V (state G). Finally, the XRD pattern at state H (Fig. 4c) and Zn 2p XPS spectrum (Fig. S7) shows that the $Zn_4SO_4(OH)_6{\cdot}0.5H_2O$ formed on the surface of the carbon fiber totally decomposes into the electrolyte during the subsequent charge process to the maximum 1.9 V cell voltage [22,34].

The formation of $Zn_4SO_4(OH)_6{\cdot}0.5H_2O$ during the discharge processes is accompanied by H^+ insertion to achieve a neutral charge system [34,51]. To confirm the likely H^+ adsorption/desorption in ACC, solid-state ^1H NMR of the ACC cathode at different states were studied, namely OCV, full discharge to 0 V (State G), and subsequent charge to 1.9 V (State H). The ^1H NMR results are shown in Fig. 4d. A chemical shift is observed at 3.159 ppm, which is ascribed to H^+ adsorption on the surface of ACC [34]. This peak is absent at OCV and fully charged state (State H), which shows the successful extraction of H^+ during the charge process. In-situ Raman spectroscopy (Fig. 4e and f) is used to track the electrosorption/desorption process of H^+ in ACC [52–54]. An ACC//Zn ZIHC is fabricated, and the Raman spectra are recorded using a time interval of 200 s during GCD processes at 3 mA cm^{-2} in the potential range of 0–1.9 V (Fig. 4e). The intensities of the D and G bands reduce gradually during the first charge process from OCV to 1.9 V, then progressively increase during the discharge process to 0 V, and finally reduce during the recharge process to 1.9 V (Fig. 4f). The continual changes in the intensity of D and G bands at the different charge and discharge states are due to the hydrogen adsorption/desorption process on the surface of ACC. Finally, Raman shifts are observed for the D and G bands during the charge/discharge processes, confirming the electro-adsorption/desorption of H^+ on the surface of ACC. The in-situ Raman spectroscopy results are in full agreement with previous reports on hydrogen storage in carbon materials and further corroborates with the ^1H NMR results [54].

The charge storage process in the zinc anode is studied using ex-situ XRD and SEM (Fig. 5). The zinc foil anode retains the smooth surface (Fig. 5c) after the first full charge to 1.9 V (state A). Next, stripping of Zn from the surface of the anode is observed during the discharge to 1.0 V (Fig. 5d) and further continues until the full discharge (Fig. 5e). The (002) and (004) peaks increase in intensity with an accompanying decrease in the (101) peak during the discharge process (Fig. 5b). Upon recharging the fabricated ZIHC to the maximum cell potential of 1.9 V, a smooth Zn surface is re-obtained (Fig. 5f). $Zn_4SO_4(OH)_6{\cdot}0.5H_2O$, $Zn(OH)_2$, or ZnO are not formed on the surface of the Zn foil anode during charge/discharge. The Na_2SO_4 electrolyte additive inhibits the formation of $Zn_4SO_4(OH)_6{\cdot}0.5H_2O$ nanoflakes/nanosheets while the neutral pH of the electrolyte prevents the formation of $Zn(OH)_2$. On the contrary, $Zn_4SO_4(OH)_6{\cdot}0.5H_2O$ is formed on the Zn foil in $ZnSO_4$ electrolyte (Fig. S8). The detailed reaction mechanism taking place in the zinc-ion HSC can be detailed as below:

Positive electrode

Physical adsorption of SO_4^{2-}: $C//SO_4^{2-} \leftrightarrow C + SO_4^{2-}$

Chemical adsorption (Zn^{2+}, H^+): $ACC\cdots O + Zn^{2+}/H^+ + e^- \leftrightarrow ACC\cdots O\cdots Zn/ACC\cdots O\cdots H$

Negative electrode: $Zn \leftrightarrow Zn^{2+} + 2e^-$

Compared with other reported ZIHCs, the fabricated device presents ~100% Coulombic efficiency, which is attributable to the highly reversible charge storage mechanism in the positive/negative electrodes [25,47]. More importantly, the reduced ESR is vital in realizing high rate charge storage, improved rate capability, and superior gravimetric power density of the ZIHC, which may be attributed to the addition of Na_2SO_4 in the electrolyte. To confirm the contribution of Na_2SO_4 to the charge storage in ACC, different symmetric supercapacitors are fabricated using 1 M Na_2SO_4, 1 M $ZnSO_4$, and 1 M Na_2SO_4/1 M $ZnSO_4$ as the electrolytes (Fig. S9). As shown in Fig. S9d, the rate capability in the

1–50 mA cm^{-2} current range follows a trend of Na_2SO_4 (67%) > $ZnSO_4/Na_2SO_4$ (42%) > $ZnSO_4$ (24%). The IR drop (Fig. S10) also follows a similar trend and reveals that the charge storage process taking place in the carbon-positive material is extremely limited at high rates in the $ZnSO_4$ electrolyte [22,25,27,28]. In addition, the cycling performance of a zinc symmetric cell was tested for 90 h using the two different electrolytes to demonstrate the advantage of the 1 M $ZnSO_4$/1 M Na_2SO_4 electrolyte. As shown in Fig. S11, the zinc symmetrical cell exhibited slightly superior cycling performances compared with the conventional $ZnSO_4$ electrolyte.

Finally, to demonstrate the universality of this electrolyte modification strategy, ZIHCs are fabricated using a 1 M LiCl/1 $ZnSO_4$ electrolyte. LiCl has been extensively used for testing the performance of carbon materials. The ZIHC achieves a high energy density of 112.95 Wh kg^{-1} and a maximum power density of 125.5 kW kg^{-1} in LiCl/$ZnSO_4$ electrolyte, far exceeding the performance in 1 M $ZnSO_4$ electrolyte (Fig. S12).

4. Conclusion

In summary, we have demonstrated using ACC as an example that the charge storage process in ZIHCs is severely limited at high rates in $ZnSO_4$ electrolytes, and this affects the specific capacity, rate capability, power density, and energy density. The addition of 1 M Na_2SO_4 in $ZnSO_4$ electrolyte significantly boosts the charge storage in the cathode at high rates and shields the zinc foil anode from the growth of Zn dendrites, resulting in lower resistances and improved electrochemical performances. The fabricated ACC//Zn ZIHCs with 1 M $ZnSO_4$/1 M Na_2SO_4 electrolyte exhibit energy densities of 100 and 20 Wh kg^{-1} at power densities of 50 and 1692 W kg^{-1}, respectively. In contrast, the ZIHCs with traditional $ZnSO_4$ electrolyte deliver energy densities of 100 and 4.5 Wh kg^{-1}, revealing the limited energy density at high rates. By using NMR, in-situ Raman, and XRD, we successfully prove the electro-adsorption/desorption of H^+ contribution to the charge storage of ZIHCs. The H^+ adsorption/desorption process precedes the formation of the $Zn(OH)_2$ analogs and is crucial in extending the voltage window to 1.9 V with excellent Coulombic efficiency. We believe our work may bring a promising strategy to develop high-energy, high-rate, and high-power aqueous Zn-ion supercapacitors through electrolyte modification.

Author contribution

Kwadwo Asare Owusu: Conceptualization; Data curation; Formal analysis; Investigation; Methodology; Software; Visualization; Roles/Writing- Original Draft; Writing- Reviewing & Editing; **Xuelei Pan**: Data curation; Formal analysis; Software; **Ruohan Yu**: Data curation; Formal analysis; Software; **Longbing Qu**: Conceptualization; Methodology; **Ziang Liu**: Visualization; **Zhaoyang Wang**: Data curation; Formal analysis; **Muhammed Tahir**: Roles/Writing- Reviewing & Editing; **Waqas Ali Haider**: Roles/Writing-Reviewing & Editing; **Liang Zhou**: Conceptualization; Supervision; Validation; Visualization; Writing- Reviewing & Editing; Investigation; Methodology; Project administration; **Liqiang Mai**: Conceptualization; Supervision; Validation; Resources; Funding acquisition.

Declaration of Competing Interest

The authors declare that they have no known competing financial interests or personal relationships that could have appeared to influence the work reported in this paper.

Acknowledgements

This work was supported by the National Natural Science Foundation of China (51832004, 51521001), the National Key Research and Development Program of China (2016YFA0202603), the Programme of Introducing Talents of Discipline to Universities (B17034), China, Foshan Xianhu Laboratory of the Advanced Energy Science, China and Technology Guangdong Laboratory (XHT2020-003), China.

Appendix A. Supplementary data

Supplementary data to this article can be found online at https://doi.org/10.1016/j.mtener.2020.100529.

References

[1] Y.L. Lu, N. Nakicenovic, M. Visbeck, A.S. Stevance, Nature 520 (2015) 432–433.
[2] P. Simon, Y. Gogotsi, Nat. Mater. 7 (2008) 845–854.
[3] F.F. Nerini, J. Tomei, L.S. To, I. Bisaga, P. Parikh, M. Black, A. Borrion, C. Spataru, V.C. Broto, G. Anandarajah, B. Milligan, Y. Mulugetta, Nat. Energy 3 (2018) 10–15.
[4] N. Choudhary, C. Li, J. Moore, N. Nagaiah, L. Zhai, Y.W. Jung, J. Thomas, Adv. Mater. 29 (2017) 1605336.
[5] V. Augustyn, P. Simon, B. Dunn, Adv. Mater. 7 (2014) 1597–1614.
[6] M. Salanne, B. Rotenberg, K. Naoi, K. Kaneko, P.L. Taberna, C.P. Grey, B. Dunn, P. Simon, Nat. Energy 1 (2016) 16070.
[7] M.R. Lukatskaya, B. Dunn, Y. Gogotsi, Nat. Commun. 7 (2016) 12647.
[8] Z. Fan, J. Yan, T. Wei, L. Zhi, G. Ning, T.Y. Li, F. Wei, Adv. Funct. Mater. 21 (2011) 2366–2375.
[9] J. Yan, Q. Wang, T. Wei, Z.J. Fan, Adv. Energy Mater. 4 (2014) 1300816.
[10] G.G. Amatucci, F. Badway, A. Du Pasquier, T. Zheng, J. Electrochem. Soc. 148 (2001) A930–A939.
[11] K.A. Owusu, L.B. Qu, J.T. Li, Z.Y. Wang, K.N. Zhao, C. Yang, K.M. Hercule, C. Lin, C.W. Shi, Q.L. Wei, L. Zhou, L.Q. Mai, Nat. Commun. 8 (2017) 14264.
[12] Z.C. Zhuang, Y. Li, J.Z. Huang, Z.L. Li, K.N. Zhao, Y.L. Zhao, L. Xua, L. Zhou, L.V. Moskaleva, L.Q. Mai, Sci. Bull. 64 (2019) 617–624.
[13] M. Xu, Q. Yu, Z.H. Liu, J.S. Lv, S.T. Lian, B. Hu, L.Q. Mai, L. Zhou, Nanoscale 10 (2018) 21604–21616.
[14] X. Wang, S. Kajiyama, H. Iinuma, E. Hosono, S. Oro, I. Moriguchi, M. Okubo, A. Yamada, Nat. Commun. 6 (2015) 6544.
[15] M.R. Lukatskaya, B. Dunn, Y. Gogotsi, Nat. Commun. 7 (2016) 12647.
[16] J. Ding, H.L. Wang, Z. Li, K. Cui, D. Karpuzov, X.H. Tan, A. Kohandehgan, D. Mitlin, Energy Environ. Sci. 8 (2015) 941–955.
[17] H.W. Wang, C.R. Zhu, D.L. Chao, Q.Y. Yan, H.J. Fan, Adv. Mater. 29 (2017) 1702093.
[18] Y.F. Ma, H.C. Chang, M. Zhang, Y.S. Chen, Adv. Mater. 27 (2015) 5296–5308.
[19] L.B. Dong, W. Yang, W. Yang, Y. Li, W.J. Wu, G.X. Wang, J. Mater. Chem. A 7 (2019) 13810–13832.
[20] P. He, M.Y. Yan, G.B. Zhang, R.M. Sun, L.N. Chen, Q.Y. An, L.Q. Mai, Adv. Energy Mater. 7 (11) (2017) 1601920.
[21] L.Y. Zhang, L. Chen, X.F. Zhou, Z.P. Liu, Adv. Energy Mater. 5 (2015) 1400930.
[22] L.B. Dong, X.P. Ma, Y. Li, L. Zhao, W.B. Liu, J.Y. Cheng, C.J. Xu, B.H. Li, Q.H. Yang, F.H. Kang, Energy Storage Mater. 13 (2018) 96–102.
[23] M.Y. Yan, P. He, Y. Chen, S.Y. Wang, Q.L. Wei, K.N. Zhao, X. Xu, Q.Y. An, Y. Shuang, Y.Y. Shao, K.T. Mueller, L.Q. Mai, J. Liu, J.H. Yang, Adv. Mater. 30 (2018) 1703725.
[24] G.Q. Sun, H.S. Yang, G.F. Zhang, J. Gao, X.T. Jin, Y. Zhao, L. Jiang, L.T. Qu, Energy Environ. Sci. 11 (2018) 3367–3374.
[25] X.P. Ma, J.Y. Cheng, L.B. Dong, W.B. Liu, J. Mou, L. Zhao, J.J. Wang, D.Y. Ren, J.L. Wu, C.J. Xu, F.Y. Kang, Energy Storage Mater. 20 (2019) 335–342.
[26] L.B. Dong, W. Yang, W. Yang, H. Tian, Y.F. Huang, X.L. Wang, C.J. Xu, C.Y. Wang, F.Y. Kang, G.X. Wang, Chem. Eng. J. 384 (2020) 123355.
[27] H. Wang, M. Wang, Y.B. Tang, Energy Storage Mater. 13 (2018) 1–7.
[28] Z. Liu, G.Z. Li, T. Cui, A. Borodin, C. Kuhl, F. Endres, J. Solid State Electrochem. 22 (2018) 91–101.
[29] Y.Y. Lu, Z.W. Li, Z.Y. Bai, H.Y. Mi, C.C. Ji, H. Pang, C. Yu, J.S. Qiu, Nanomater. Energy 66 (2019) 104132.
[30] P.G. Liu, W.F. Liu, Y.P. Huang, P.L. Li, J. Yan, K.Y. Liu, Energy Storage Mater. 25 (2020) 858–865.
[31] H.L. Pan, Y.Y. Shao, P.F. Yan, Y.W. Cheng, K.S. Han, Z.M. Nie, C.M. Wang, J.H. Yang, B. Bhattacharya, K.T. Mueller, J. Liu, Nat. Energy 1 (2016) 16039.
[32] S. Higashi, S.W. Lee, J.S. Lee, K. Takechi, Y. Cui, Nat. Commun. 7 (2016) 11801.
[33] N. Zhang, F.Y. Cheng, Y.C. Liu, Q. Zhao, K.X. Lei, C.C. Chen, X.S. Liu, J. Chen, Nat. Commun. 138 (2016) 12894–12901.
[34] F. Wan, L.L. Zhang, X. Dai, X.Y. Wang, Z.Q. Niu, J. Chen, Nat. Commun. 9 (2018) 1656.
[35] J.S. Ko, M.D. Donakowski, M.B. Sassin, J.F. Parker, D.R. Rolison, J.W. Long, MRS Commun. 9 (2019) 99–106.

[36] J.S. Ko, M.B. Sassin, J.F. Parker, D.R. Rolison, J.W. Long, Sustain. Energy Fuels 2 (2018) 626–636.
[37] F. Beguin, V. Presser, A. Balducci, E. Frackowiak, Adv. Mater. 26 (2014) 2219–2251.
[38] K.A. Owusu, L.B. Qu, Z.Y. Wang, L.B. Qu, Z. Liu, J.A.-A. Mehrez, Q.L. Wei, L. Zhou, L.Q. Mai, Chin. Chem. Lett. 31 (2020) 1620–1624.
[39] Z.J. Liu, Z.H. Zhao, Y.Y. Wang, S. Dou, D.F. Yan, D.D. Liu, Z.H. Xia, S.Y. Wang, Adv. Mater. 29 (2017) 1606207.
[40] W. Wang, W.Y. Liu, Y.X. Zenng, Y. Han, M.H. Minghao, X.H. Liu, Y.X. Tong, Adv. Mater. 27 (2015) 3572–3578.
[41] G.M. Wang, H.Y. Wang, X.H. Lu, Y.C. Ling, M.H. Yu, T. Zhai, Y.X. Tong, Y. Li, Adv. Mater. 26 (2014) 2676–2682.
[42] X. Wang, C.X. Lu, H.F. Peng, X. Zhang, Z.K. Wang, G.K. Wang, J. Power Sources 324 (2016) 188–198.
[43] L.J. Zhang, Y.Z. Jiang, L.W. Wang, C. Zhang, S.X. Liu, Electrochem. Acta 196 (2016) 189–196.
[44] M. Yu, Y.Y. Han, J. Li, L.J. Wang, Chem. Eng. J. 317 (2017) 493–502.
[45] H.H. Zhong, Y. Luo, S. He, P.G. Tang, D.G. Li, N. Alonso-Vante, Y.J. Feng, ACS Appl. Mater. Interfaces 9 (2017) 2541–2549.
[46] C.J. Lei, Y. Wang, Y. Hou, P. Liu, J. Yang, T. Zhang, X.D. Zhuang, M.W. Chen, B. Yang, L.C. Lei, C. Yuan, M. Qiu, X.L. Feng, Energy Environ. Sci. 12 (2019) 149–156.
[47] S.L. Wu, Y.T. Chen, T.P. Jiao, J. Zhou, J. Cheng, B. Liu, S.R. Yang, K.L. Zhang, W.J. Zhang, Adv. Energy Mater. (2019) 1902915.
[48] L.B. Qu, Y.L. Zhao, A.M. Khan, C.H. Han, K.M. Hercule, M.Y. Yan, X.Y. Liu, W. Chen, D.D. Wang, Z.Y. Cai, K.N. Zhao, X.L. Zheng, L.Q. Mai, Nano Lett. 15 (2015) 2037–2044.
[49] S.M. Chen, L.T. Ma, K. Zhang, M. Kamruzzaman, J.A. Zapien, J. Mater. Chem. A 7 (2019) 7784–7790.
[50] L. He, Y. Liu, C.Y. Li, D. Yang, W.G. Wang, W.Q. Yan, W.B. Zhou, Z.X. Wu, L.L. Wang, Q.H. Huang, Y.S. Zhu, Y.H. Chen, L.J. Fu, X.H. Hou, Y.P. Wu, ACS Appl. Energy Mater. 2 (2019) 5835–5842.
[51] J.H. Huang, Z. Wang, M.Y. Hou, X.L. Don, Y. Liu, Y.G. Wang, Y.Y. Xia, Nat. Commun. 9 (2018) 2906.
[52] K. Fic, A. Platek, J. Piwek, J. Menzel, A. Slesinski, P. Bujewska, P. Galek, E. Frackowiak, Energy Storage Mater. 22 (2019) 1–14.
[53] S. Leyva-Garcia, E. Morallón, D. Cazorla-Amorós, F. Béguin, D. Lozano-Castelló, Carbon 69 (2014) 401–408.
[54] D. Qu, J. Power Sources 179 (2008) 310–316.